A comparison study of a solar active-region eruptive filament and a neighboring non-eruptive filament

Chao-Wei Jiang[1,2*], Shi-Tsan Wu[2,3], Xue-Shang Feng[1] and Qiang Hu[2,4]

[1] SIGMA Weather Group, State Key Laboratory for Space Weather, National Space Science Center, Chinese Academy of Sciences, Beijing 100190, China; *cwjiang@spaceweather.ac.cn*
[2] Center for Space Plasma & Aeronomic Research, The University of Alabama in Huntsville, Huntsville, AL 35899, USA
[3] Department of Mechanical & Aerospace Engineering, The University of Alabama in Huntsville, Huntsville, AL 35899, USA
[4] Department of Space Sciences, The University of Alabama in Huntsville, Huntsville, AL 35899, USA

Abstract Solar active region (AR) 11283 is a very magnetically complex region and it has produced many eruptions. However, there exists a non-eruptive filament in the plage region just next to an eruptive one in the AR, which gives us an opportunity to perform a comparison analysis of these two filaments. The coronal magnetic field extrapolated using our CESE–MHD–NLFFF code reveals that two magnetic flux ropes (MFRs) exist in the same extrapolation box supporting these two filaments, respectively. Analysis of the magnetic field shows that the eruptive MFR contains a bald-patch separatrix surface (BPSS) co-spatial very well with a pre-eruptive EUV sigmoid, which is consistent with the BPSS model for coronal sigmoids. The magnetic dips of the non-eruptive MFRs match Hα observation of the non-eruptive filament strikingly well, which strongly supports the MFR-dip model for filaments. Compared with the non-eruptive MFR/filament (with a length of about 200 Mm), the eruptive MFR/filament is much smaller (with a length of about 20 Mm), but it contains most of the magnetic free energy in the extrapolation box and holds a much higher free energy density than the non-eruptive one. Both the MFRs are weakly twisted and cannot trigger kink instability. The AR eruptive MFR is unstable because its axis reaches above a critical height for torus instability, at which the overlying closed arcades can no longer confine the MFR stably. On the contrary, the quiescent MFR is very firmly held by its overlying field, as its axis apex is far below the torus-instability threshold height. Overall, this comparison investigation supports that an MFR can exist prior to eruption and the ideal MHD instability can trigger an MFR eruption.

Key words: magnetic fields — Sun: corona — Sun: filaments — Sun: eruptions

1 INTRODUCTION

As a leading cause of space weather, coronal mass ejections (CMEs) are closely correlated with solar filament eruptions. A recent statistical study shows that more than 70 percent of filaments eventually erupt and result in CMEs (McCauley et al. 2015). Therefore, it is of great importance for space weather forecasting to understand why the filaments erupt and predict when they are likely to erupt. To answer these questions, one needs information about a key parameter, the invisible coronal magnetic field behind the filaments, which is believed to play the primary role in supporting the filaments and characterizing their stability.

Accordingly, a variety of theoretical models have been proposed to explain the initiation of filament eruptions with the coronal magnetic disruption as the basis (see, e.g., Forbes et al. 2006; Aulanier et al. 2010; Schmieder et al.

2013; Aulanier 2014, and references therein). The physical mechanisms causing the eruption can be classified as, e.g., the breakout model (Antiochos et al. 1999), the tether cutting model (Moore et al. 2001) as well as ideal magnetohydrodynamic (MHD) instabilities (e.g., kink instability and torus instability, Hood & Priest 1981; Velli et al. 1990; Török et al. 2004; Török & Kliem 2005; Kliem & Török 2006) and the non-ideal MHD instabilities (e.g. tearing mode instability given by Wu et al. 2000).

It is understood that pre-eruption, the stressed core field in the corona is usually kept stable by an envelope/overlying the field anchored strongly at the photosphere, thus the essence of all eruption initiation models is to find how the balance between the outward magnetic pressure of the core field and the downward magnetic tension of the overlying field can be broken. Hence, Antiochos et al. (1999) proposed the breakout model based on a quadrupolar magnetic field configuration, and that the

eruption is triggered by reconnection at a coronal null point above the sheared core arcade, which removes the overlying flux and then allows the core to escape, similar to a streamer and flux rope model (Wu & Guo 1997; Wu et al. 1997). The tether cutting model usually refers to a complete process of the formation and eruption of a magnetic flux rope (MFR) from an initial simple, sheared bipolar magnetic arcade (Moore & Roumeliotis 1992; Moore et al. 2001). In a strongly sheared bipolar field, a current sheet forms above the photospheric polarity inversion line (PIL) and results in tether-cutting reconnection between the arcade field lines, which progressively transforms the arcade core into a rising twisted MFR. The reconnection is further forced by converging motions toward the PIL, flux diffusion and cancelation in the photosphere (Amari et al. 2003a,b; Linker et al. 2003). Such processes continuously add flux to the MFR and in turn weaken the photospheric anchorage below the MFR, until at some instant, the remaining arcade tethers are too weak to prevent the eruption of the MFR. In this case, it is different from the breakout model since the magnetic reconnection works at low altitude below the stressed field. The ideal MHD instabilities mainly include the kink instability and the torus instability for an MFR. The kink instability occurs if the twist, a measure of the number of windings of the field lines around the rope axis, exceeds a critical value, leading to a helical deformation of the MFR's axis (Török & Kliem 2005; Török et al. 2010). The torus instability (Kliem & Török 2006) is equivalent to a catastrophic loss of equilibrium (Forbes 1990; Forbes & Isenberg 1991; Kliem et al. 2014) that occurs when the MFR reaches an unstable threshold determined by the decay speed of the envelope/overlying magnetic field that stabilizes the MFR. On the other hand, the non-ideal MHD instability was examined by Wu et al. (2000), who investigated the formation of observed plasma blobs (Sheeley et al. 1997) with multi-polarity magnetic field topology due to tearing mode instability.

Of all the mentioned theoretical models, it appears that only the one with ideal MHD-instability can provide a set of specific parameters, i.e., the twist degree of the MFR and/or the decay index of the envelope field, that quantifies the condition when the magnetic configuration might erupt. Thus this is a very attractive advantage that promises to make itself most popular in the community of space weather research. We note that such a model is built up on a basic element, the MFR, which is assumed to exist prior to the eruption. This is indeed supported by several lines of evidence. The coronal sigmoids often appearing in CME-productive active regions (ARs) (Rust & Kumar 1996; Hudson et al. 1998; Canfield et al. 1999) indicate sheared and twisted magnetic configurations, and thus an MFR, prior to the eruption; furthermore, the MFR can explain well the supporting of filaments because the dip structure in MFR provides a reservoir where the cool dense material can be held against gravity (Mackay et al. 2010; Guo et al. 2010b; Su et al. 2011), and thus a long-lasting quiescent filament strongly suggests a correspondingly last-

ing MFR. On the other hand, with different numerical techniques and force-free models, many authors have successfully reconstructed MFRs from vector magnetograms that are consistent with the observation signatures like sigmoids and filaments (Canou & Amari 2010; Cheng et al. 2010; Guo et al. 2010b; Jing et al. 2010; Guo et al. 2013; Jiang et al. 2014a,b; Ruan et al. 2014; Amari et al. 2014); moreover, direct observations of the pre-existence of MFR have also been frequently reported in the Solar Dynamics Observatory (SDO) era with the help of high-quality multi-wavelength data from the Atmospheric Imaging Assembly (AIA) (Cheng et al. 2012; Zhang et al. 2012; Li & Zhang 2013a,b,c; Patsourakos et al. 2013; Yang et al. 2014; Chen et al. 2014). Furthermore, ideal MHD-instability theory has been extensively applied in the investigations of filament eruptions (Romano et al. 2003; Williams et al. 2005; Green et al. 2007; Schrijver et al. 2008; Liu 2008; Guo et al. 2010a; Cheng et al. 2011; Nindos et al. 2012; Xu et al. 2012; Liu et al. 2012; Cheng et al. 2013; Kliem et al. 2013; Jiang et al. 2014a; Amari et al. 2014), and it is noteworthy that many successful and failed eruption events are consistent with the theory, in particular the theoretical threshold values for instability are matched strikingly well in the data-constrained/data-driven modeling results (e.g., Kliem et al. 2013; Guo et al. 2010a; Jiang et al. 2014a, 2013).

In this paper we provide further evidence for the pre-existence of MFR and the ideal MHD-instability mechanism for the eruption of MFR by a comparison study of an eruptive filament in AR 11283 and a nearby non-eruptive filament. Both filaments have been studied independently in our previous work (Jiang et al. 2014a,b) using coronal field reconstructions, but here by comparing them with each other, we provide further insight into the different nature between the eruptive and non-eruptive filaments. We find that both of the filaments are supported by coronal MFR. The MFR corresponding to the AR eruptive filament is much smaller compared with the non-eruptive MFR, but contains significantly more magnetic free energy than the non-eruptive one. Both MFRs are weakly twisted and cannot trigger kink instability. The eruptive MFR is unstable because its axis reaches above a critical height for torus instability, while the non-eruptive MFR is very firmly held by its overlying field, as its axis apex is far below the torus-instability threshold height.

2 OBSERVATIONS AND CORONAL MAGNETIC FIELD MODEL

AR 11283 produced two X-class flares (an X2.1 on 2011 September 6 and an X1.8 on September 7), which have motivated many studies (Wang et al. 2012; Petrie 2012; Zharkov et al. 2013; Feng et al. 2013; Jiang et al. 2013, 2014a; Ruan et al. 2014; Liu et al. 2014; Shen et al. 2014; Xu et al. 2014; Zhang et al. 2015). Here we investigate the coronal configuration on September 6 before the X2.1 flare. The SDO/AIA observed that an S-shaped small-scale filament (with length of about 20 Mm) formed in the core of the AR and erupted at the onset of the flare at 22:12 UT,
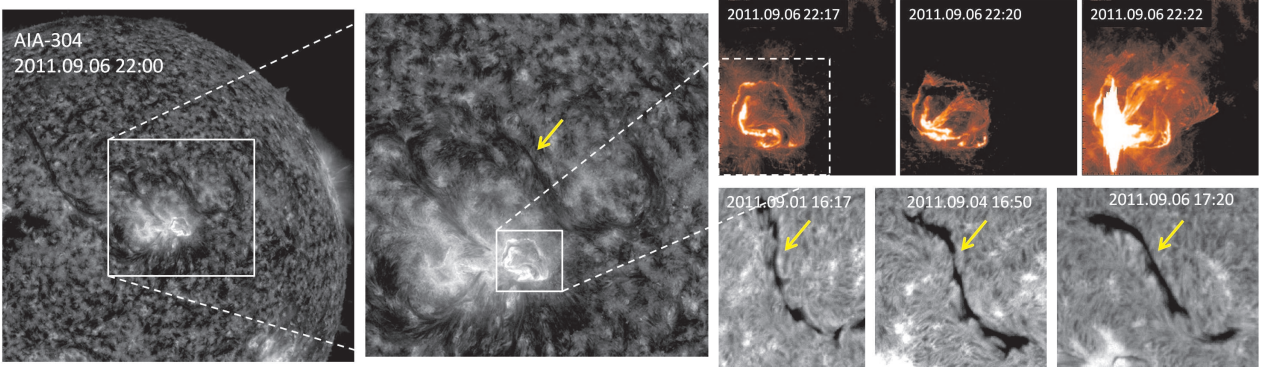
Fig. 1 *Left*: a large AIA-304 image at 22:00 UT on September 6, showing the location of AR 11283. *Middle*: closer view of the region. The top-right small panels show the eruptive process of the AR filaments with three time snapshots, and the bottom-right small panels show the Big Bear Solar Observatory (BBSO) Hα observations of the non-eruptive, large filament, with the arrows pointing to the main body of the filament as indicated in the AIA-304 image.

with impulsive rising of the filament matter, as shown in Figure 1. On the other hand, in the northwest of the AR, there is a large filament, the main body of which, as seen in Hα, shows a slightly inverse-S shape with a length up to 200 Mm. The large filament exists stably for many days, and survives during the eruption of the small one, although its main body is very close to the flare site. The right-bearing filament barbs as seen in the Hα indicate that the non-eruptive filament should be related with a left-handed twisted MFR, which is contrary to the eruptive one.

To investigate the coronal magnetic field that supports the filaments, we have modeled the pre-flare magnetic field using our CESE–MHD–NLFFF code with input from the SDO/Helioseismic and Magnetic Imager (HMI) vector magnetogram (see also Jiang et al. 2014b). The code is based on the MHD relaxation approach and is implemented by an advanced conservation-element/solution-element (CESE) space-time scheme (Jiang et al. 2010). We solve a set of zero-beta simplified MHD equations with a fictitious frictional force to control the relaxation process. The code is in line with our 3D MHD Data-driven Active Region Evolution model (Wu et al. 2006; Jiang et al. 2012, 2013; Wu et al. 2014), which has been well tested for reproducing both the slow quasi-static evolution and extremely fast eruption process in the large-scale corona. The present model is performed in a Cartesian coordinate system with the z axis along the normal vector of the solar surface.

3 RESULTS AND ANALYSIS

3.1 Comparison of Coronal Magnetic Field Model with Observations

The coronal field model displays two MFRs with opposite helicity in the same extrapolation box: a small one with right-hand twist (see a close-up view in Fig. 2) corresponding to the eruptive AR filament, and a large one with left-hand twist corresponding to the non-eruptive intermediate filament. To validate the model result, we car-

ried out a detailed comparison of the magnetic field and its derived features with the observations of structures related to the filament. In particular, for the large-scale filament, the Hα observation is compared with the magnetic dips in its MFR, since there is a good Hα image of the filament spine and barbs, and these structures are believed to consist of cold matter collected in the magnetic dips. For the small AR filament, since observations with Hα do not have adequate resolution, comparison of its MFR field lines with an extreme ultraviolet (EUV) sigmoid that is closely co-spatial with the AR filament provides a better way for our validation of the modeling.

In the left panels of Figure 2, we compare the magnetic dips with the large Hα filament. The magnetic dips are visualized by showing part of the isosurface ($B_z = 0$) with $\boldsymbol{B} \cdot \nabla B_z > 0$ (i.e., locations where the field lines are concave up). The dips are also pseudo-colored by the value of height for a better representation of the long extended dip structure, since there is a large amount of localized fragmentation of dips (shown in deep blue) that is very close to and on the photosphere (i.e., bald patches). Evidently, the long extended dip reaches above 30 Mm, exhibiting an inverse S-shape, reproducing the main body of the filament. In particular, there are small-scale magnetic dips emanating from the spine, and they match the filament barbs strikingly well. The results are in line with and provide evidence for the MFR-dip model for filaments and their barbs.

The right panels of Figure 2 show the comparison of the magnetic field lines of the AR MFR with the sigmoid observed in AIA-94 (temperature of 6.3 MK). The sigmoid has a thin and enhanced forward-S shape, indicating a right-hand twist. We find that this MFR has a bald patch separatrix surface (BPSS), as shown by the thick white lines in the figure, which is the MFR's outmost surface that touches the photosphere. The BP is a part of the PIL on the photosphere where the transverse field crosses from negative to positive polarity (note that the BP is directly derived from the vector magnetogram), and the BPSS consists of
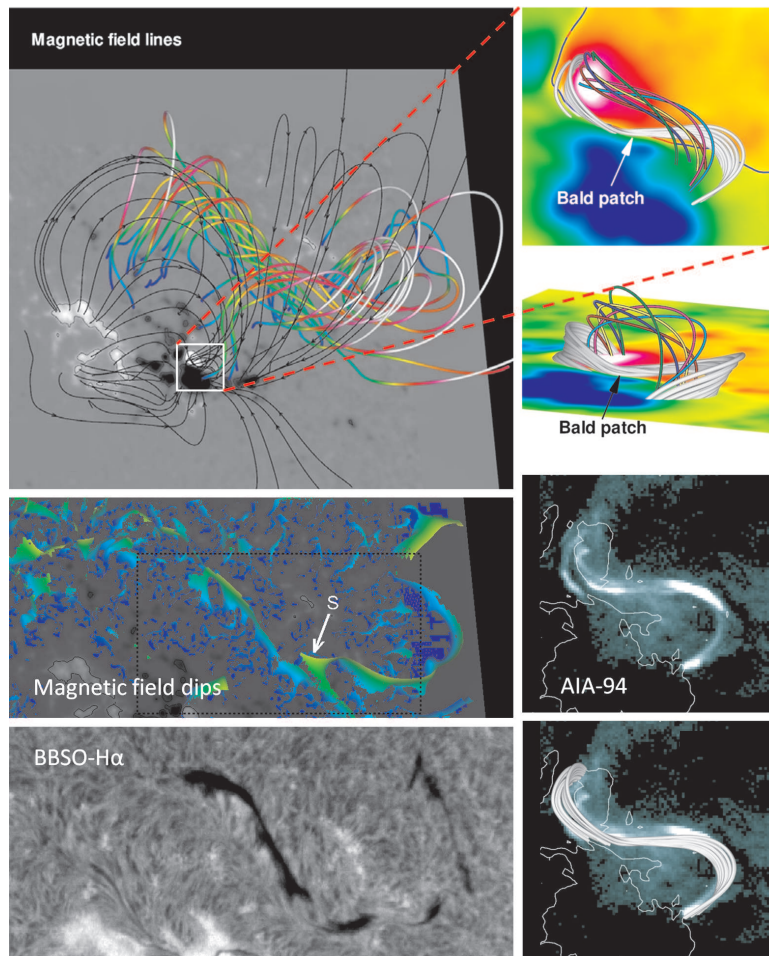
Fig. 2 *Left*: Comparison of the magnetic dips of the large MFR with the large filament seen in BBSO Hα (adapted from Jiang et al. 2014b). The top is the magnetic field lines, the middle is the magnetic dips (pseudo-colored by the height from 0 to 60 Mm), and the bottom is the Hα image. The dashed box outlines the region of the main body of the filament. The arrow 'S' identifies a separation of the filament. *Right*: Comparison of the BPSS of the AR MFR with the AIA-94 sigmoid (adapted from Jiang et al. 2014a). The background color images show the photospheric magnetic flux distribution (white for 500 G and blue for −500 G), with the PIL denoted by the curved line. The BPSS consists of the field lines plotted as white thick rods, which graze the photospheric surface at the BP. The colored field lines are sampled near the MFR axis. The bottom panels are the AIA-94 image of the sigmoid with the same field-of-view as the top ones. In the last panel the BPSS field lines are overlaid on the AIA image.

all the field lines that pass through the BP. Theoretical study suggests that a strong current sheet can form in the BPSS of MFR and produces enhanced heating along the surface, which manifests itself as the X-ray or EUV sigmoid (Titov & Démoulin 1999). The most important result is that the observed sigmoid coincides with the BPSS field lines, but not with those near the rope axis (the thick colored lines in the figure). Such fact not only supports the BPSS current sheet model for sigmoid brightening, but also confirms the validation of our model.

3.2 Magnetic Energy Distributions

In Figure 3 and Table 1 we compare the magnetic energy distributions of the two MFRs related to the filaments. Figure 3 shows the free energy density integrated along the

z axis, namely

$$E_{\text{free}}(x,y) = dxdy \int \frac{B^2 - B_{\text{pot}}^2}{8\pi} dz . \tag{1}$$

As can be seen, compared with the intermediate region, the free energy is significantly stronger in the sunspot regions, i.e., the AR core, because of the strong magnetic flux there. For the large MFR, there is also clearly a channel of enhanced free energy along the corresponding filament, with the central section possessing the strongest free energy. Table 1 gives a comparison of different energy contents and mean free-energy density of the two MFRs. Although the two MFRs are involved in the entire magnetic configuration, they can be regarded as independent of each other according to the magnetic topology. As shown by Jiang et al. (2014a), the AR eruptive MFR is formed
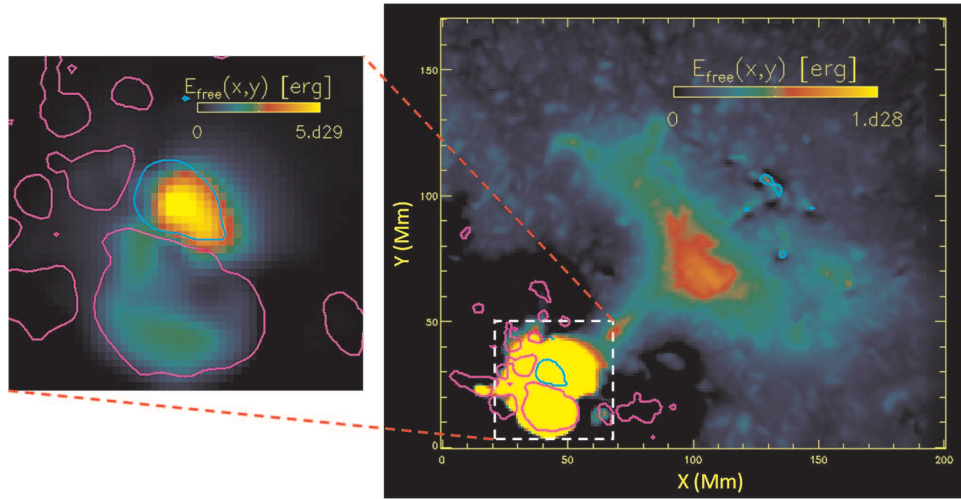
Fig. 3 Free energy density integrated along the z axis. The contour lines represent B_z of -500 G (*pink*) and 500 G (*cyan*). The small box in the large field of view shown in the right panel is identified as the AR core, i.e., for the separated volume of the eruptive MFR, which is enlarged in the left panel. Since the energy is much stronger in the AR core than in the intermediate region, different scales of the energy distribution are used in the two panels.
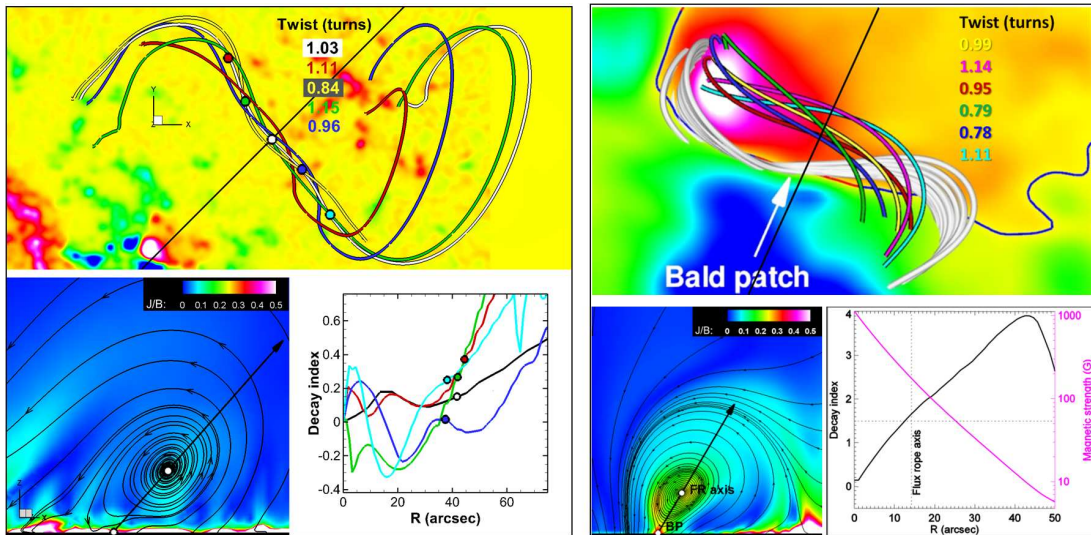
Fig. 4 Analysis of the stability of the two MFRs: left panels are for the non-eruptive one (adapted from Jiang et al. 2014b) and right panels are for the eruptive one (adapted from Jiang et al. 2014a). The top panels show the twist degrees of the MFRs, which are calculated for several sampled field lines around the rope axis (which is represented by the white line for the large MFR in the left panel and yellow line for the small MFR in the right panel). The bottom panels show the results for decay index. The central cross sections for the two MFRs are shown respectively, and these cross sections are vertically sliced along the black lines shown in the top panels. The streamlines in these cross sections show the 2D field-line tracing of the slices, which forms helical lines centered at the axis of the MFR. The thick lines with arrows that point from the bottom to the helix center (i.e., the rope axis) represent the paths along which the decay index is computed. Since the axis of the large MFR is very long, the decay index is calculated at four more points along its axis, which are denoted by the colored circles in the left panels.

with the emerging of a new positive sunspot into the large negative flux region, and a magnetic null-point fan separatrix surface (like a dome) exists between the pre-existing system and the newly emerged one. The AR MFR with its overlying flux system is localized below the fan surface with a height of about 30 Mm. As such, we roughly separate the two MFRs in the full extrapolation volume using a small box with height of 30 Mm encompassing the eruptive MFR as shown in Figure 3, and the rest of the volume for the non-eruptive one. Then the different energy contents are computed using these separated volumes for the two MFRs. Notably, although in spatial size the eruptive MFR is much smaller than the non-eruptive one, it contains most of the magnetic free energy. Consequently the free energy

Table 1 Comparison of Magnetic Energy Contents for the Two MFRs

	AR Eruptive MFR	Non-eruptive MFR
Total energy	3.67×10^{32} erg	1.52×10^{32} erg
Potential energy	2.63×10^{32} erg	1.28×10^{32} erg
Free energy	1.04×10^{32} erg	0.24×10^{32} erg
Ratio of free energy to potential energy	40%	19%
Field volume	4.66×10^{4} Mm^3	2.98×10^{6} Mm^3
Mean free energy density	2230 erg cm^{-3}	8 erg cm^{-3}

density of the eruptive MFR is far higher than that of the non-eruptive one. The ratio of free energy to potential energy shows that the non-potentiality of the AR MFR field is also significantly higher than that of the non-eruptive one. These comparisons indicate a higher possibility of disruption for the AR MFR than for the other one.

3.3 Stabilities of the Flux Ropes

To further explain why the AR filament erupts immediately whereas the large filament can stay stable, we study the stabilities of the MFRs with the 3D coronal field in the context of ideal MHD instabilities. Theoretical models and simulations suggest that a coronal MFR (i.e., MFR with footpoints line tied to the photosphere) confined by an overlying potential arcade is subject to two kinds of ideal instabilities, i.e., kink instability and torus instability. Kink instability occurs if the twist degree of the MFR, denoted by T_n, which measures the number of windings of the field lines around the rope axis, exceeds a critical value. This threshold value is estimated to be roughly $1.5 \sim 2$, according to several studies (Fan & Gibson 2003; Török et al. 2004; Török & Kliem 2005). The torus instability occurs when the outward expansion of an MFR due to its "hoop force" can no longer be confined by the overlying field (also referred to as the external field) if the external field decreases sufficiently fast. A decay index is defined as

$$n(R) = -\frac{\partial(\ln B_e)}{\partial(\ln R)} \tag{2}$$

to characterize how fast the external field B_e decreases with distance R from the photosphere, and it has been found that if the apex of the rope axis reaches a location with the decay index greater than a threshold n_c, the MFR system is unstable. This value n_c is expected to lie in the range of $1.1 \lesssim n_c \lesssim 2$ from a series of investigations (Bateman 1978; Kliem & Török 2006; Török & Kliem 2007; Fan & Gibson 2007; Schrijver et al. 2008; Démoulin & Aulanier 2010; Aulanier et al. 2010). One should bear in mind that these threshold values for instabilities may change depending on many factors, e.g., the specific shape of the flux rope and the magnetic environments. Thus they should be used with caution in realistic cases.

The twist degree T_n of a force-free MFR can be simply quantified by integrating the force-free factor $\alpha = \boldsymbol{J} \cdot \boldsymbol{B}/B^2$ along a given field line, namely,

$$T_n = \frac{1}{4\pi} \int \alpha dl \tag{3}$$

(Berger & Prior 2006; Inoue et al. 2011, 2013). In the upper panels of Figure 4, we show the results for several field lines around the rope axis. Since in the realistic case the MFR is actually a bundle of field lines winding around each other, it is difficult to precisely locate the axis of the rope like in an analytic or idealized model. We thus approximately find the rope axis by first making a central cross section of the MFR, which is a vertical slice cutting roughly through the middle of the MFR in a direction perpendicular to the photospheric central PIL, and then assuming the rope axis to be the field line passing through the center of the helical shapes formed by the poloidal flux of the rope (as shown in the bottom panels of Fig. 4). The results show that the twist degrees of both MFRs are very close to one turn, although their different field lines have slightly different values of twist. Such values of twist are below the thresholds of kink instability that have been reported. Moreover, we have not observed a clear rotation or writhe in the erupting AR filament as it rises, which would otherwise occur in the eruption of kinked MFR. We concluded that neither of the filaments can trigger kink instability.

Several points need to be clarified with respect to studying the torus instability based on computing the decay index. First, since it is difficult to separate the external field from the total field in the model, we use the potential field that corresponds to the same magnetogram as an approximation of the external field, following Fan & Gibson (2007) and Aulanier et al. (2010). Second, as mentioned, the axis apex of the MFR is hard to precisely determine, and we thus approximately locate it at the center of the helical shapes formed by the poloidal flux of the rope in the central cross section. For the large filament that has a rather long axis, we compute the decay index at four more points along its axis. Third, since the MFR and overlying field configuration is inclined with respect to the radial (or vertical) direction, it will be more reasonable to compute the decay index along a path approximately following the inclination of the system than along the vertical direction. Last, because the field parallel to the rising direction actually does not contribute to the inward confining force, the decay index is only computed for the perpendicular component of the potential field (Cheng et al. 2011; Nindos et al. 2012). Accordingly, we compute the decay index for the two MFRs and compare them in the bottom panels of Figure 4. As can be seen, the non-eruptive MFR is located at heights with decay index smaller than 0.5, which is far below the threshold for torus instability, thus it is very

firmly held by its overlying field. On the other hand, the AR MFR reaches slightly above the height with decay index of 1.5, which is the threshold of torus instability found by Török & Kliem (2007) and Aulanier et al. (2010) using idealized numerical simulations. Thus our result supports the threshold value as 1.5, and suggests that the quick eruption of the AR MFR is due to torus instability.

4 CONCLUSIONS

We performed a comparative analysis of an eruptive filament in AR 11283 and a nearby non-eruptive filament in the intermediate region using a zero-beta MHD-relaxation model for nearly force-free extrapolation (Jiang & Feng 2013). The extrapolated coronal magnetic field based on the measured vector magnetogram given by SDO/HMI shows that the two MFRs support the two filaments. Validation of the modeled magnetic field is performed by comparing it with EUV and Hα observations, which shows that the eruptive MFR contains a BPSS spatially coinciding with the pre-eruptive sigmoid, and the non-eruptive MFR has magnetic dips matching the shape of the non-eruptive filament. By comparing the MFRs with each other, the following physical characteristics are found: (i) The eruptive filament is only one tenth the size of the non-eruptive filament. (ii) The amount of free energy of the eruptive filament is five times that of the non-eruptive one. (iii) The mean free energy density of the eruptive filament is more than two orders of magnitude larger than the non-eruptive one. (iv) Both MFRs are weakly twisted, thus they could not trigger the kink instability. (v) Evaluating the decay index shows that the axis of the eruptive MFR (filament) reaches above a critical height needed for torus instability, where the non-eruptive MFR is firmly held by its overlying field, as its axis apex is far below the threshold height. We suggest the measured mean free-energy density may be a good characteristic indicator for a filament eruption in addition to other properties. In summary, the energy storage and trigger mechanism are both important to filament eruptions, and it supports the idea that MFR can exist prior to eruption and the torus instability can trigger its eruption.

References

Amari, T., Canou, A., & Aly, J.-J. 2014, Nature, 514, 465

Amari, T., Luciani, J. F., Aly, J. J., Mikic, Z., & Linker, J. 2003a, ApJ, 585, 1073

Amari, T., Luciani, J. F., Aly, J. J., Mikic, Z., & Linker, J. 2003b, ApJ, 595, 1231

Antiochos, S. K., DeVore, C. R., & Klimchuk, J. A. 1999, ApJ, 510, 485

Aulanier, G. 2014, in IAU Symposium, Vol. 300, IAU Symposium, ed. B. Schmieder, J.-M. Malherbe, & S. T. Wu, 184

Aulanier, G., Török, T., Démoulin, P., & DeLuca, E. E. 2010, ApJ, 708, 314

Bateman, G. 1978, MHD Instabilities, 270 (Cambridge, Mass., MIT Press)

Berger, M. A., & Prior, C. 2006, Journal of Physics A Mathematical General, 39, 8321

Canfield, R. C., Hudson, H. S., & McKenzie, D. E. 1999, Geophys. Res. Lett., 26, 627

Canou, A., & Amari, T. 2010, ApJ, 715, 1566

Chen, H., Zhang, J., Cheng, X., et al. 2014, ApJ, 797, L15

Cheng, X., Ding, M. D., Guo, Y., et al. 2010, ApJ, 716, L68

Cheng, X., Zhang, J., Ding, M. D., Guo, Y., & Su, J. T. 2011, ApJ, 732, 87

Cheng, X., Zhang, J., Ding, M. D., et al. 2013, ApJ, 769, L25

Cheng, X., Zhang, J., Saar, S. H., & Ding, M. D. 2012, ApJ, 761, 62

Démoulin, P., & Aulanier, G. 2010, ApJ, 718, 1388

Fan, Y., & Gibson, S. E. 2003, ApJ, 589, L105

Fan, Y., & Gibson, S. E. 2007, ApJ, 668, 1232

Feng, L., Wiegelmann, T., Su, Y., et al. 2013, ApJ, 765, 37

Forbes, T. G. 1990, J. Geophys. Res., 95, 11919

Forbes, T. G., & Isenberg, P. A. 1991, ApJ, 373, 294

Forbes, T. G., Linker, J. A., Chen, J., et al. 2006, Space Sci. Rev., 123, 251

Green, L. M., Kliem, B., Török, T., van Driel-Gesztelyi, L., & Attrill, G. D. R. 2007, Sol. Phys., 246, 365

Guo, Y., Ding, M. D., Cheng, X., Zhao, J., & Pariat, E. 2013, ApJ, 779, 157

Guo, Y., Ding, M. D., Schmieder, B., et al. 2010a, ApJ, 725, L38

Guo, Y., Schmieder, B., Démoulin, P., et al. 2010b, ApJ, 714, 343

Hood, A. W., & Priest, E. R. 1981, Geophysical and Astrophysical Fluid Dynamics, 17, 297

Hudson, H. S., Lemen, J. R., St. Cyr, O. C., Sterling, A. C., & Webb, D. F. 1998, Geophys. Res. Lett., 25, 2481

Inoue, S., Hayashi, K., Shiota, D., Magara, T., & Choe, G. S. 2013, ApJ, 770, 79

Inoue, S., Kusano, K., Magara, T., Shiota, D., & Yamamoto, T. T. 2011, ApJ, 738, 161

Jiang, C. W., Feng, X. S., Zhang, J., & Zhong, D. K. 2010, Sol. Phys., 267, 463

Jiang, C., Feng, X., Wu, S. T., & Hu, Q. 2012, ApJ, 759, 85

Jiang, C., & Feng, X. 2013, ApJ, 769, 144

Jiang, C., Feng, X., Wu, S. T., & Hu, Q. 2013, ApJ, 771, L30

Jiang, C., Wu, S. T., Feng, X., & Hu, Q. 2014a, ApJ, 780, 55

Jiang, C., Wu, S. T., Feng, X., & Hu, Q. 2014b, ApJ, 786, L16

Jing, J., Tan, C., Yuan, Y., et al. 2010, ApJ, 713, 440

Kliem, B., Lin, J., Forbes, T. G., Priest, E. R., & Török, T. 2014, ApJ, 789, 46

Kliem, B., Su, Y. N., van Ballegooijen, A. A., & DeLuca, E. E. 2013, ApJ, 779, 129

Kliem, B., & Török, T. 2006, Physical Review Letters, 96, 255002

Li, L. P., & Zhang, J. 2013a, A&A, 552, L11

Li, T., & Zhang, J. 2013b, ApJ, 770, L25

Li, T., & Zhang, J. 2013c, ApJ, 778, L29

Linker, J. A., Mikić, Z., Lionello, R., et al. 2003, Physics of Plasmas, 10, 1971

Liu, C., Deng, N., Lee, J., et al. 2014, ApJ, 795, 128

Liu, R., Kliem, B., Török, T., et al. 2012, ApJ, 756, 59

Liu, Y. 2008, ApJ, 679, L151

Mackay, D. H., Karpen, J. T., Ballester, J. L., Schmieder, B., & Aulanier, G. 2010, Space Sci. Rev., 151, 333

McCauley, P. I., Su, Y. N., Schanche, N., et al. 2015, Sol. Phys., 290, 1703

Moore, R. L., & Roumeliotis, G. 1992, in Lecture Notes in Physics, Berlin Springer Verlag, 399, IAU Colloq. 133: Eruptive Solar Flares, eds. Z. Svestka, B. V. Jackson, & M. E. Machado, 69

Moore, R. L., Sterling, A. C., Hudson, H. S., & Lemen, J. R. 2001, ApJ, 552, 833

Nindos, A., Patsourakos, S., & Wiegelmann, T. 2012, ApJ, 748, L6

Patsourakos, S., Vourlidas, A., & Stenborg, G. 2013, ApJ, 764, 125

Petrie, G. J. D. 2012, ApJ, 759, 50

Romano, P., Contarino, L., & Zuccarello, F. 2003, Sol. Phys., 214, 313

Ruan, G., Chen, Y., Wang, S., et al. 2014, ApJ, 784, 165

Rust, D. M., & Kumar, A. 1996, ApJ, 464, L199

Schmieder, B., Démoulin, P., & Aulanier, G. 2013, Advances in Space Research, 51, 1967

Schrijver, C. J., Elmore, C., Kliem, B., Török, T., & Title, A. M. 2008, ApJ, 674, 586

Sheeley, N. R., Wang, Y.-M., Hawley, S. H., et al. 1997, ApJ, 484, 472

Shen, Y., Ichimoto, K., Ishii, T. T., et al. 2014, ApJ, 786, 151

Su, Y., Surges, V., van Ballegooijen, A., DeLuca, E., & Golub, L. 2011, ApJ, 734, 53

Titov, V. S., & Démoulin, P. 1999, A&A, 351, 707

Török, T., Berger, M. A., & Kliem, B. 2010, A&A, 516, A49

Török, T., & Kliem, B. 2005, ApJ, 630, L97

Török, T., & Kliem, B. 2007, Astronomische Nachrichten, 328, 743

Török, T., Kliem, B., & Titov, V. S. 2004, A&A, 413, L27

Velli, M., Hood, A. W., & Einaudi, G. 1990, ApJ, 350, 428

Wang, S., Liu, C., & Wang, H. 2012, ApJ, 757, L5

Williams, D. R., Török, T., Démoulin, P., van Driel-Gesztelyi, L., & Kliem, B. 2005, ApJ, 628, L163

Wu, S. T., & Guo, W. P. 1997, Washington DC American Geophysical Union Geophysical Monograph Series, 99, 83

Wu, S. T., Guo, W. P., & Dryer, M. 1997, Sol. Phys., 170, 265

Wu, S. T., Jiang, C., Feng, X., Hu, Q., & Liu, Y. 2014, in IAU Symposium, 300, eds. B. Schmieder, J.-M. Malherbe, & S. T. Wu, 466

Wu, S. T., Wang, A. H., Liu, Y., & Hoeksema, J. T. 2006, ApJ, 652, 800

Wu, S. T., Wang, S., & Zheng, H. 2000, Advances in Space Research, 26, 529

Xu, Y., Jing, J., Wang, S., & Wang, H. 2014, ApJ, 787, 7

Xu, Y., Liu, C., Jing, J., & Wang, H. 2012, in American Astronomical Society Meeting Abstracts, 220, American Astronomical Society Meeting Abstracts #220, #515.05

Yang, S., Zhang, J., Liu, Z., & Xiang, Y. 2014, ApJ, 784, L36

Zhang, J., Cheng, X., & Ding, M.-D. 2012, Nature Communications, 3, 747

Zhang, Q. M., Ning, Z. J., Guo, Y., et al. 2015, ApJ, 805, 4

Zharkov, S., Green, L. M., Matthews, S. A., & Zharkova, V. V. 2013, Journal of Physics Conference Series, 440, 012046